 doi:10.20944/preprints202106.0544.v1

Article

Quantitative Investigation of Radiometric Interactions Between Snowfall, Snow Cover, and Cloud Liquid Water Over Land

Zeinab Takbiri[1]*, Lisa Milani[2,3], Clement Guilloteau[4], Efi Foufoula-Georgiou[5]

[1] University of Minnesota, St. Anthony Falls Lab; takbi001@umn.edu
[2] Earth System Science Interdisciplinary Center, University of Maryland, College Park, MD;
[3] NASA Goddard Space Flight Center, Greenbelt, MD; lisa.milani@nasa.gov
[4] Department of Civil and Environmental Engineering, University of California, Irvine, Irvine, California; cguillot@uci.edu
[5] Department of Civil and Environmental Engineering, and Department of Earth System Science, University of California, Irvine, Irvine, California; efi@uci.edu
* Correspondence: takbi001@umn.edu

Abstract: Falling snow alters its own microwave signatures when it begins to accumulate on the ground making retrieval of snowfall challenging. This paper investigates the effects of snow-cover depth and cloud liquid water content on microwave signatures of terrestrial snowfall using reanalysis data and multi-annual measurements by the Global Precipitation Measurement (GPM) core satellite with particular emphasis on the 89 and 166 GHz channels. It is found that over shallow snow cover (snow water equivalent (SWE) $\leq$ 100 kgm^{-2}) and low values of cloud liquid water path (LWP $\leq 100-150$ gm^{-2}), the scattering of light snowfall (rates $\leq$ 0.5 mmh^{-1}) is detectable only at frequency 166 GHz, while for higher snowfall rates the signal can be also detected at 89 GHz. However, when SWE exceeds $\geq$ 200 kgm^{-2}and the LWP is greater than $100-150$ gm^{-2}, the emission from the increased liquid water content in snowing clouds becomes the only surrogate microwave signal of snowfall that is stronger at frequency 89 GHz than 166 GHz. The results also reveal that over high latitudes above 60° N where the SWE is greater than 200 kgm^{-2} and LWP is lower than $100-150$ gm^{-2} the microwave snowfall signal could not be detected with GPM. Our results provide quantitative insights for improving retrieval of snowfall in particular over snow-covered terrain.

Keywords: Snowfall Retrieval, Snow Water Equivalent, Cloud Liquid Water, Emissivity, Brightness Temperature, Passive Microwave, GPM

1. Introduction

Passive microwave (PMW) retrieval of snowfall is one of the most challenging components of precipitation monitoring from space, with the largest error in precipitation retrieval often related to snowfall [1–6] over snow cover [7]. Snowfall emission is almost negligible due to the low dielectric constant of ice particles, especially over emissive land surfaces. Falling snow and ice particles scatter the upwelling surface radiation at high microwave frequencies and thus decrease the observed brightness temperatures (Tb) at the top of the atmosphere. This radiometric signal, however, is much weaker than the overland rainfall scattering [8–10] and can be significantly masked due to the confounding effects of increased cloud liquid water path (LWP) during snowfall and reduced surface emissivity as a result of snow accumulation on the ground.

Snow particles have complex and variable nonspherical shapes and bulk densities. The size distribution of snowfall particles depends on numerous factors including temperature, pressure, and the level of water vapor path (WVP) supersaturation at different vertical layers of the atmosphere [11–15]. The nonspherical snow particles usually have lower densities than raindrops with equal mass, which cause them to exhibit weaker scattering [9,10,16].

Radiative transfer modeling shows that this weak scattering becomes detectable at frequencies above 80 GHz and reaches its maximum at frequencies 150 to 166 GHz [17,18]. However, in snowy clouds thermal emission from the presence of supercooled liquid water

 doi:10.20944/preprints202106.0544.v1

content can mask the already weak snowfall signal even at these high-frequency channels [19]. The warming effects of the liquid water emission in the mixed-phase clouds may even exceed the cooling effects of snowfall scattering [20] and completely mask the snowfall signal [21,22], which adds to the complexity of (light) snowfall retrievals.

The presence of snow cover on the ground is another challenge in detecting the snowfall scattering signal. Snow cover is a relatively strong scatterer at microwave frequencies above 20 GHz [23,24] and this scattering increases monotonically with frequency up to 100 GHz [25]. Increased scattering reduces the surface emissivity depending on physical and microphysical properties of snowpack such as depth, density, wetness and the distribution of grain size [24,26,27], which vary in response to the snow metamorphism [28–31]. A thicker and denser snowpack often scatters the upwelling surface emission more, especially when snow ages and develops larger and denser particles [23,27,32,33]. In addition, radiometric properties of snow cover are very sensitive to its liquid water content. For a very small amount of liquid water content of around 2%, the absorption dominates scattering and turns the snowpack to almost a blackbody radiator [34]. The combination of the explained radiometric processes has two important consequences, which add to the complexity of PMW snowfall retrievals. First, there is a likelihood that the snow cover and snowfall microwave signatures become very similar [2,35,36]. Second, the low emissivity of dry snow cover can significantly weaken the already weak snowfall scattering [6,37–39] or vanish it completely.

Radiative transfer modeling of both snowfall and snow-cover has large complexity under diverse environmental conditions over land with large variability over temporal and spatial scales, and requires many input parameters [40]. Most radiative transfer modeling has been conducted assuming that the snowfall particles are spherical [1,15], and single scattering theories can approximate their scattering. The discrete-dipole approximation is also used to account for the non-spherical shape of snowfall ice particles [41,42]. Nevertheless, snowfall radiative transfer models can often account only for a limited number of snowfall particle shapes [43,44] and lack the ability to properly address bulk scattering of a snowfall profile throughout the atmospheric column [45]. Additionally, modeling of the emission signal of the supercooled liquid water content in snowing clouds is still not well parameterized especially at frequencies above 31 GHz [15,46]. Using the Rayleigh approximation in the absence of precipitation for water droplets larger than 0.2 mm [47] calculated the microwave absorption of supercooled liquid water at 21 and 31 GHz and found that this absorption strongly depends on cloud temperatures. Thus, the resulting absorption derived from common dielectric models significantly deviates during the snowfall at temperatures below 270 K mainly due to poor representations of the primary relaxation frequency of water.

The snow cover scattering below 100 GHz can be explained by the Born approximation approach [48] that partially accounts for the near-field radiation produced by adjacent snow grains, using the low-frequency practical media theory [49]. More recently, in order to extend the range to larger particles and higher-frequencies, Grody [27] proposed the use of a quasi-crystalline approximation to bridge the gap between small- and large-size snow grains. However, the radiative transfer modeling of snow cover effects is not conducted for frequencies above 150 GHz [30] in which the primary snowfall retrieval bands are located in the PMW spectra. The uncertainty of this high-frequency approximation is often quite larger than that at lower frequencies because the optical parameters of snow cover become less frequency-dependent and saturated as the particle diameter approaches the wavelength.

Clearly, complexities of radiative transfer modeling are amplified when it comes to modeling snowfall over snow cover, accounting for the presence of cloud liquid water content, where there is significant heterogeneity in the characterization of the initial and boundary conditions at a global scale. The Global Precipitation Measurement (GPM) Mission PMW observations can help to unpack these relatively unknown radiometric interactions and to provide some important insights into PMW snowfall retrievals. A

 doi:10.20944/preprints202106.0544.v1

recent empirical study conducted by [38] using coincidental CloudSat and GPM observations found that cloud liquid water emission increases the brightness temperatures up to 10 K at 166 GHz, and usually even more at 89 GHz. Besides these interesting findings, previous studies have not considered the synergistic effect of atmospheric LWP and surface-accumulated Snow Water Equivalent (SWE) on the snowfall signal.

The goal of this paper is to quantify the radiometric effects of snow cover and cloud liquid water content on the microwave signatures of snowfall at high-frequency channels, largely focusing on observations from the GPM core satellite. The findings of this paper push the understanding of the land-atmospheric effects one step further, investigating the conditions in which the passive radiometric signal of snowfall is affected and thus cannot be detected without considering a priori data about SWE and LWP. In particular, the following main questions are addressed:

- What are the scattering contributions of snowfall and snow cover on the observed Tbs for different snowfall intensities and SWE?
- Why, when, where and to what extent the liquid water content of clouds can mask the snowfall signals over snow-covered surfaces?
- Under which boundary conditions can the snow cover obscure the snowfall signatures?
- Are there any particular conditions that completely mask the snowfall PMW signal?

To answer the above questions, we extract and isolate the contributions of snowfall scattering, snow cover scattering, and LWP emission in observed Tbs as a function of snowfall rate (sr), LWP, and SWE. To that end, we rely on multi-year coincident GMI [7] and DPR data [50], as well as ancillary information of SWE, LWP, and temperature. As previously noted, we mostly focus on the high-frequency channels at 89 and 166 GHz that are critical for snowfall retrieval.

Section 2 describes the products and data used for the analyses. Section 3 discusses the observed climatology of SWE, LWP, surface, and atmospheric temperature using their marginal and spatial distributions at different snowfall rates. By removing atmospheric effects, Section 4 quantifies the clear-sky microwave emissivity of the snow-covered surfaces as a function of SWE. In Section 5 we add the effects of LWP emissions, and finally in Section 6 we complete the radiative budget adding the snowfall component. Discussion and conclusions are presented in Section 7 and 8.

2. Data and Products

The GPM core observatory, launched in 2014, carries the dual-frequency precipitation radar (DPR) and the GPM GMI allowing for active and passive, colocated in space and time, observations [51,52]. Snowfall events and their radiometric signatures are extracted using the level-2 precipitation phase data from the GPM DPR product (2ADPR-V06) at the normal-sensitivity (NS) scan [53] and the calibrated GPM microwave imager (GMI) Tbs (1C-R GMI V05) [7]. Total precipitable water (TPW) is also from the GPM active microwave product (2ADPR-V06). The PMW measurements are from the GMI with 13 channels ranging from 10 to 183 GHz. In the DPR product, both Ka- and Ku-band (35.5 and 13.6 GHz respectively) radar reflectivity values are used to estimate the precipitation rate to reduce the uncertainty of single band retrievals. The combination of active and passive observations provides a unique opportunity to understand unknown radiometric properties of solid precipitation [54] over snow-covered surfaces at frequencies above 100 GHz. The surface temperature (T_{skin}), 2-meter temperature (T_{2m}), the cloud LWP, vapor water paths (VWP), and ice water path (IWP) are all obtained from the Modern-Era Retrospective analysis for Research and Applications version 2 (MERRA-2) [55]. The average air temperature, also derived from the DPR atmospheric state environmental ancillary information (2ADPRENV), comes originally from the Japan Meteorological Agency (JMA) Global ANALysis (GANAL). This temperature is the average air temperature from 0 to 20 km at a 250-m resolution and will be called T_{air}, hereafter in this paper. The extent of snow-covered surfaces is determined from the Interactive Multisensor Snow and Ice Mapping System (IMS) at 1-km spatial resolution

Preprints (www.preprints.org) | NOT PEER-REVIEWED | Posted: 22 June 2021 doi:10.20944/preprints202106.0544.v1

Table 1: Abbreviations, data, and products.

Variable	Symbol	Unit	Source
89 GHz brightness temperature	Tb_{89}	K	1C-R GMI V05 satellite observation product
166 GHz brightness temperature	Tb_{166}	K	1C-R GMI V05 satellite observation product
1833 GHz brightness temperature	Tb_{1833}	K	1C-R GMI V05 satellite observation product
1837 GHz brightness temperature	Tb_{1837}	K	1C-R GMI V05 satellite observation product
Snowfall rate	sr	mmh^{-1}	2ADPR-V06 satellite observation product
Total precipitable water vertically integrated on 0-20 km	TPW	kgm^{-2}	2ADPR-V06 satellite observation product
Skin temperature	T_{skin}	K	MERRA-2 reanalysis
2-m temperature	T_{2m}	K	MERRA-2 reanalysis
Snow cover extent	IMS	Dimensionless	United States National Ice Center
Snow water equivalent on the ground	SWE	kgm^{-2}	MERRA-2 reanalysis
Cloud liquid water path	LWP	gm^{-2}	MERRA-2 reanalysis
Ice water path	IWP	gm^{-2}	MERRA-2 reanalysis
Water vapor path	WVP	gm^{-2}	MERRA-2 reanalysis
Air temperature averaged on 0-20 km	T_{air}	K	GANAL analysis
Clear sky land emissivity	ε_s	dimensionless	$\varepsilon_s = \frac{Tb_s}{T_{skin}}$
Cloud liquid water emissivity	ε_{lwp}	dimensionless	$\varepsilon_{lwp} = \frac{Tb_{obs} - \varepsilon_s T_{skin}}{T_{air}}$
Total atmospheric emissivity	ε_a	dimensionless	$\varepsilon_a = \varepsilon_{sr} + \varepsilon_{lwp}$

[56], while SWE is obtained from the hourly MERRA-2 product [57, M2T1NXLND] at a $0.625^\circ \times 0.5^\circ$ spatial resolution. All data and variables used/calculated in this study, their units, and sources are listed in Table 1.

In this paper, we only focus on events over dry snow cover, where both T_{skin} and T_{2m} are below 0 °C. Surface is considered as snow-covered when the IMS binary product indicates snow cover and the SWE from MERRA-2 reanalysis is greater than zero. We considered data from January 2015 to December 2020 over the Northern Hemisphere (NH) land surfaces. MERRA-2 data are linearly interpolated onto the scanning time of the GPM overpasses and re-gridded onto the DPR grid using the nearest neighbor interpolation. In the explained methodology no information is lost at the expense of some redundancy in the coincident data. The binary snow-covered/no snow-covered IMS 1-km data is converted to 4-km binary snow-cover data using nearest neighbour (to find the IMS pixels in each 4-km by 4-km 2ADPR grid) and the majority vote rule ($> 50\%$).

3. North Hemisphere climatology of Snow Cover and Cloud Liquid Water

The radiometric signal of snowfall, snow cover, and cloud LWP are tightly intertwined at high microwave frequencies ($\geq$ 89 GHz). The snowflakes and snow cover grains both scatter the upwelling surface emission (cooling effect), while the cloud LWP content adds to this emission (warming effect). An increase in SWE leads to an increased scattering volume of the snow cover and thus to a decrease of the surface emissivity and observed Tbs. An increased scattering of snowing clouds should further decrease the Tbs especially for high snowfall rates. The snowfall scattering, however, becomes relatively less significant at larger SWE values because of a reduced background emission, which adds to the complexities of snowfall retrievals.

3.1. Marginal and Spatial Distribution of Snow Cover in terms of Snow Water Equivalent

To unravel the effects of SWE and LWP on the quality of snowfall retrievals, we first need to investigate the frequency distribution of these variables. Fig. 1a shows the positively skewed marginal probability distribution function (PDF) of SWE over the NH. The median and the mean are 41 kgm^{-2} and $\sim$ 74 kgm^{-2} respectively. The histogram is color coded to show the mean T_{skin} for each 25 kgm^{-2} SWE interval. SWE values

Preprints (www.preprints.org) | NOT PEER-REVIEWED | Posted: 22 June 2021 doi:10.20944/preprints202106.0544.v1

between $30 - 300$ kgm^{-2} show colder temperatures than the tail segments with the lowest temperature occurring at about 75–100 kgm^{-2} . Fig. 1a also shows that these SWE values with lowest temperature on average occur at latitudes 54-57° N. It is calculated by averaging latitudes associated with the all SWE data fall in each SWE bins. To understand the reasons for the T_{skin} behaviour, we look into the maps of the SWE annual probability of occurrence and the corresponding mean T_{skin} shown in Fig. 1c–h. It is worth noting that here the mean refers to the entire NH in the histogram in each SWE bin, while it refers to the single grid box (1-deg resolution) in the maps.

SWE values between 0–40 kgm^{-2}(Fig. 1c) are consistently displayed over land surfaces that are likely to receive snowfall ($> 30°$ N). The highest probability of occurrence is over the High Mountain Asia and southern Siberian Plateau, where T_{skin} is visibly colder than the surrounding areas (<265 K , Fig. 1f). However, the area with colder T_{skin} (green area in Fig. 1f) with high occurrence frequency of 0–40 kgm^{-2}SWE values (red area in Fig. 1c) is much smaller than the warmer T_{skin} regions (orange and red areas in Fig. 1f). Therefore, despite its higher probability of occurrence, the latter dominates the T_{skin} mean values and we see a relatively high T_{skin} in the SWE PDF for low SWE values (0–40 kgm^{-2}) in Fig. 1a.

The intermediate SWE values (40–100 kgm^{-2}, Fig. 1d) are spread mostly over higher latitudes ($> 45°$ N) that are likely to receive higher snowfall amounts throughout the year. The most frequent values are over cold surfaces ($T_{skin} < 250$ K), clustered over central Canada in the vicinity of the southwest coasts of the Hudson Bay and eastern of the Central Siberian Plateau. Cold temperatures of these highly frequent regions in this case dominate the climatology of the SWE values and explain the observed T_{skin} depressions for SWE values of $40 - 100$ kgm^{-2} in the marginal SWE distribution in Fig. 1a.

Finally, SWE values greater than 100 kgm^{-2} are more frequent over latitudes above 56° N (Fig. 1a), especially over the Pacific Coast Ranges of northern British Columbia, North East Canada, Ural Mountains, Kjolen Mountains of Norway, and Verkhoyansk Range in Russian Far East (Fig. 1e), where the mean T_{skin} varies between 250–260 K (Fig. 1h). High values of SWE usually occur during late winter/early spring due to snow accumulation when the temperature begins to increase, justifying the slightly higher mean T_{skin} compared to the 40–100 kgm^{-2} SWE interval. This higher mean temperature concurrent with larger SWE values (> 100 kgm^{-2}) over Pacific Coast Ranges and Ural Mountains can weaken or mask the expected incremental increase in the scattering signal of snow cover in these regions.

3.2. Marginal and Spatial Distribution of Cloud Liquid Water

The parameterization of the cloud liquid water content over the snow-covered land surface requires an accurate characterization of the sub-grid distribution of thermodynamic variables such as cloud phase, cloud type, cloud vertical structure, precipitation occurrence, and geolocation. To this end, we investigate the marginal PDF and the spatial distribution of the multiyear LWP with respect to the snowfall occurrence as well as snowfall rate (sr) over dry snow covered areas (defined as snow cover where both T_{skin} and T_{2m} are below zero). The distribution of LWP as a function of T_{air} and sr is presented in Fig. 2. Similar to Fig. 1, here the mean refers to the entire NH in the histograms in each LWP bin, while it refers to the single grid box in the maps.

Fig. 2a-c shows the histogram of the LWP values corresponding to the orbit-level DPR observations using nearest-neighbor interpolation to match the 2ADPR-V06 resolution. The colors in the histograms shown in Fig. 2a and Fig. 2b represent the multi-year average of T_{air} for each LWP bin size of 14.2 gm^{-2}. For non-precipitating clouds ($sr = 0$, Fig. 2a) and over dry snow cover — when usually the cold weather regime dominates — the PDF of LWP has a large positive skewness (γ= 1.91). This significantly skewed distribution indicates a high probability of occurrence of supercooled liquid clouds containing low LWP values. The mean and standard deviation are 36 gm^{-2} and 46 gm^{-2}, respectively. In the snowing atmosphere ($sr > 0$, Fig. 2b), the PDF skewness decreases to $\gamma = 0.08$ and the

Preprints (www.preprints.org) | NOT PEER-REVIEWED | Posted: 22 June 2021 doi:10.20944/preprints202106.0544.v1

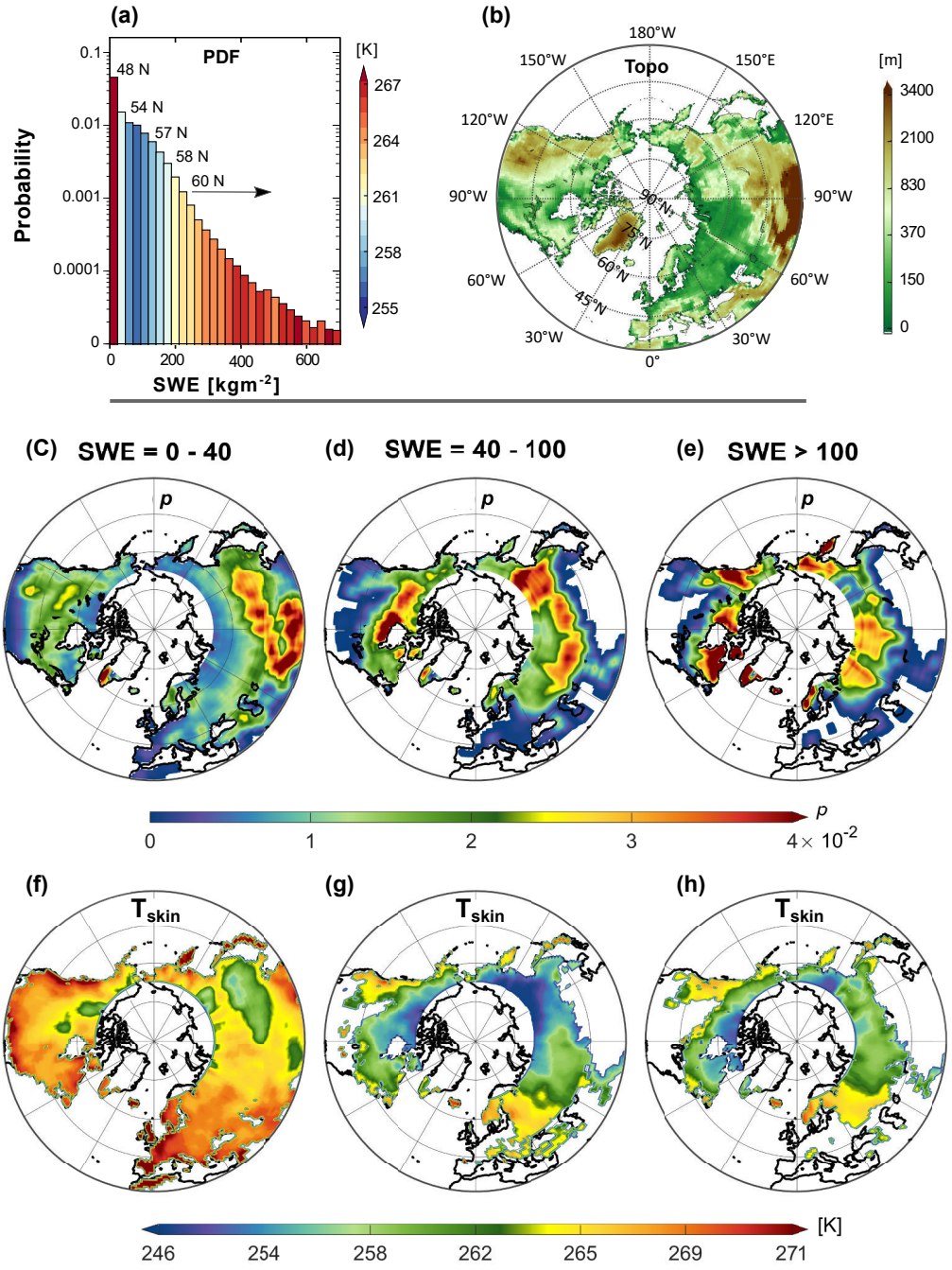

Figure 1. Marginal probability distribution function (PDF) of multi-year Snow Water Equivalent (SWE in kgm^{-2}) and T_{skin} (in degree K) dependency (a), NH topographic map (b), SWE spatial probability of occurrence (p) (c-e), and T_{skin} (f-h) at 1-deg resolution for three SWE intervals in kgm^{-2}. Note the color scale in (a) and (b) indicates the average T_{skin} (K) for each SWE bin and the elevation (m), respectively. Note that the y-axis in (a) is logarithmic.

mean increases to $\sim$ 140 gm^{-2}, indicating the existence of a larger amount of supercooled liquid droplets in clouds.

During snowfall events, the most frequent values of LWP is around 140-160 gm^{-2}, while the occurrence probability of extremely low LWP values ($<$ 20 gm^{-2}) is below 0.0015 (Fig. 2b). Larger values of LWP occur more frequently at warmer air temperatures as the moisture holding capacity of the atmosphere is higher and more ice water can turn into liquid [58]. However, the increasing rate of LWP with temperature is not constant.

Preprints (www.preprints.org) | NOT PEER-REVIEWED | Posted: 22 June 2021 doi:10.20944/preprints202106.0544.v1

This is because different values of LWP occur at different vertical heights. The database developed by Kubota *et al.* [59] using the global cloud system resolving model for the GPM/DPR algorithm revealed that over land the LWP increases with precipitation. Our analysis in Fig. 2c confirms the evolution of the LWP probability distribution as a function of snowfall rate. The PDFs become less skewed and wider as the mean moves from 80 gm^{-2} ($sr = 0 - 0.5$ mmh^{-1}, blue curve) to 200 gm^{-2} ($sr = 4 - 8$ mmh^{-1}, black curve).Also, we observe that for $sr > 2$ mmh^{-1} the LWP distribution does not change or shift noticeably.

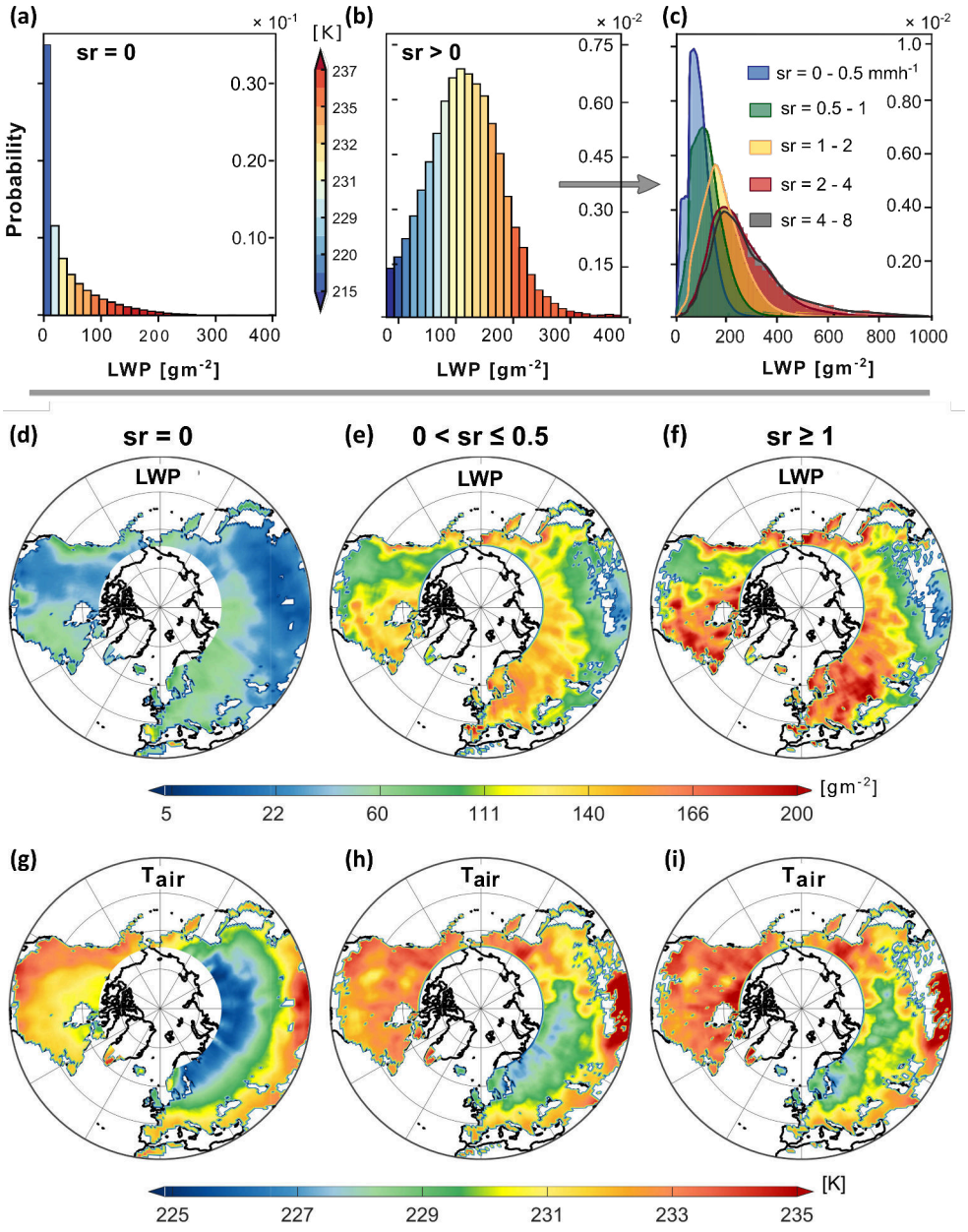

Figure 2. The effects of different overland snowfall rates (sr) on frequency and spatial distribution of cloud LWP over the NH: probability distribution functions of LWP for $sr = 0$ (a), $sr > 0$ (b) and $0 < sr < 8$ mmh^{-1} (c); spatial distribution of the mean LWP (d–f), and the T_{air} (g–i) for non-precipitating (d,g), $0 < sr \leq 0.5$ mmh^{-1} (e,h) and $sr \geq 1$ (f, i). The histograms are color coded to represent corresponding mean T_{air} temperatures. Note that the color represents the multi-year average of T_{air} for each LWP bin (in the top row), the multi-year gridded average of LWP (second row), and the multi-year gridded average of T_{air} (bottom row).

Preprints (www.preprints.org) | NOT PEER-REVIEWED | Posted: 22 June 2021 doi:10.20944/preprints202106.0544.v1

To understand the spatial variations of LWP from non-snowing to snowing atmospheres we stratified our dataset based on different snowfall intensities. Fig. 2 shows the spatial pattern of mean LWP (d-f) and T_{air} (g-i) for three different scenarios: sr = 0 (no snowfall), $0 < sr \leq 0.5$ mmh^{-1} (about 40 percentile), and $sr \geq 1$ mmh^{-1} (95 percentile) — over dry snow cover. The average LWP and its corresponding T_{air} increase with the increase of sr. This is because the predominant snowfall-temperature relationship is positive at mid- to high-latitudinal regions during the cold-weather regime in winter [60]. The snowfall warming feedback significantly increases the T_{air} over North America, Siberia, and East Asia where colder temperatures were observed in absence of precipitation, while temperatures at lower latitudes remain almost unchanged (Fig. 2g-i). Fig. 2 also shows that the rate of increase in both LWP and T_{air} with snowfall rate is not uniform over the entire NH. The increase of T_{air} specifically is observed over the Siberian plateau and the northern Canada. The increase of LWP over these regions concurrently occurs with increase of atmospheric temperature both of which increase the emissivity and could significantly mask the Tb response to the increase in snowfall scattering.

3.3. Radiometric Effects of Snow Cover and Cloud Liquid Water on GPM brightness temperature

To understand the effects of the observed complex climatology of snow cover, temperature, LWP, and morphology of snow cover grain on GPM brightness temperatures, the averages of high-frequency Tbs are calculated as a function of SWE at different LWP values. Fig. 3 shows the average NH Tbs as a function of SWE and cloud LWP in the absence of precipitation. For brevity, we focus on the vertical polarization (V-pol) channels as the response pattern is similar in the horizontally polarized (H-pol) ones (not shown here). We would expect a monotone decrease in the snow cover emissivity pattern as the SWE increases for frequencies below 100 GHz [23,24,48]. However, results show that Tb values do not monotonically decrease and there is a clear inversion in the Tb spectra. As shown in Fig. 3, Tb values approach a minimum at around 70–100 kgm^{-2} and begin to increase for SWE > 120 kgm^{-2} . This anomalous spectra was previously observed in SSM/I frequency channels at 19, 37, and 85 GHz [30] and explained as a radiometric response of the snowpack to its crystalline structure changes when the mean grain size increases [27]. Among the GMI channels, both the 89 and 166 GHz ones are almost equally sensitive to the increase of SWE while the 183 GHz is the least sensitive, because of the atmospheric water vapor emission. On average, for a 1 kgm^{-2} increase in SWE, the Tb decreases about 0.5 K at 89 and 166 GHz, 0.2 K at 183 ± 3 GHz, and 0.4 K at 183 ± 7 GHz. It is worth noting that the observed anomaly follows the climatology of T_{skin} for different SWE values (Fig. 3f). The snow cover metamorphic changes on grain size and the snow cover temperature climatology are not independent, therefore the observed scattering signal is a response to both seasonal and spatial variations of snow cover emissivity and T_{skin} as shown in Fig. 1.

Since the crystalline structure of the snow pack is a function of its metamorphic changes, the observed anomaly shows a seasonal dependence. The Tb seasonal dependence here is calculated by averaging the time stamp of Tb values at each SWE bin. Fig. 3 shows that the maximum snow cover scattering occurs during the early winter. As the T_{skin} and the snow mean grain size increase toward the late spring, the scattering signal begins to decay even though the SWE continues to increase. It is important to note that this seasonal pattern impacts the quality of snowfall microwave retrievals. In particular, since strong snow cover scattering can weaken the snowfall signal, we expect larger uncertainties on PMW snowfall retrievals on early winter when the snow cover is fresh and the SWE is less than 100 kgm^{-2}.

The analysis also shows warmer Tbs for increasing frequencies which is in contradiction with the known surface emissivity spectra of snow cover [23]. Within the analyzed range of SWE (0 - 400 kgm^{-2}), the 166 GHz channel is more than 5 K warmer than the 89 GHz one, while the overall expectation is that the high-frequency channels must be colder due to stronger snow cover scattering [23,24,48]. This inverted spectrum was observed in lower frequency channels of the SSM/I sensor and is known to be due to the

 doi:10.20944/preprints202106.0544.v1

formation of a dense layer of snow crust [30]. Hewison and English [61] also argues that this phenomenon could be due to the mean behavior of the snow cover temperature profile, that is often colder at the bottom layers.

Finally, an increase of cloud LWP can completely mask scattering effects of snow cover. This masking effect is shown in Fig. 3 as we see the curves are flatter for higher LWP (moving from blue to red lines). This is expected because of the climatology of LWP and T_{air} observed in Fig. 2, e.g., larger values of LWP occur at warmer T_{air}, on average. Fig. 3a–d shows that for LWP > 150 gm^{-2} , there is almost no response to changes on SWE. Moreover, the SWE value associated with the maximum scattering (Tb minimum) increases as the cloud LWP increases. The reason could be while the maximum snow cover scattering occurs in early winter (Oct-Dec) over dry snow the emission of cloud liquid water is stronger from mid to late winter (Jan-Mar) [62]. This is attributed to the fact that the temperature begins to gradually increase from mid to late winter. This masking effect is also frequency-dependent. In particular, when the scattering signal of snow cover is maximum, the Tb_{89} GHz increases about 5 K more than the Tb_{166} GHz in response to an increase of 200 gm^{-2} in cloud LWP. We also observe that the difference between the channel spectra shrinks for high (200 kgm^{-2}) and low (2.5 kgm^{-2}) values of LWP (Fig. 3e) — revealing the nonlinear effects of LWP on snow cover high-frequency signatures.

Now that we discussed and showed the complex radiometric effects of SWE and LWP climatology and snow-cover grain morphology on the GPM brightness temperatures, the question is how we can isolate these correlated effects on the Tb signal of snowfall in order to improve snowfall passive retrieval from GPM frequency channels. We approach this by calculating emissivity in the next sections.

Preprints (www.preprints.org) | NOT PEER-REVIEWED | Posted: 22 June 2021 doi:10.20944/preprints202106.0544.v1

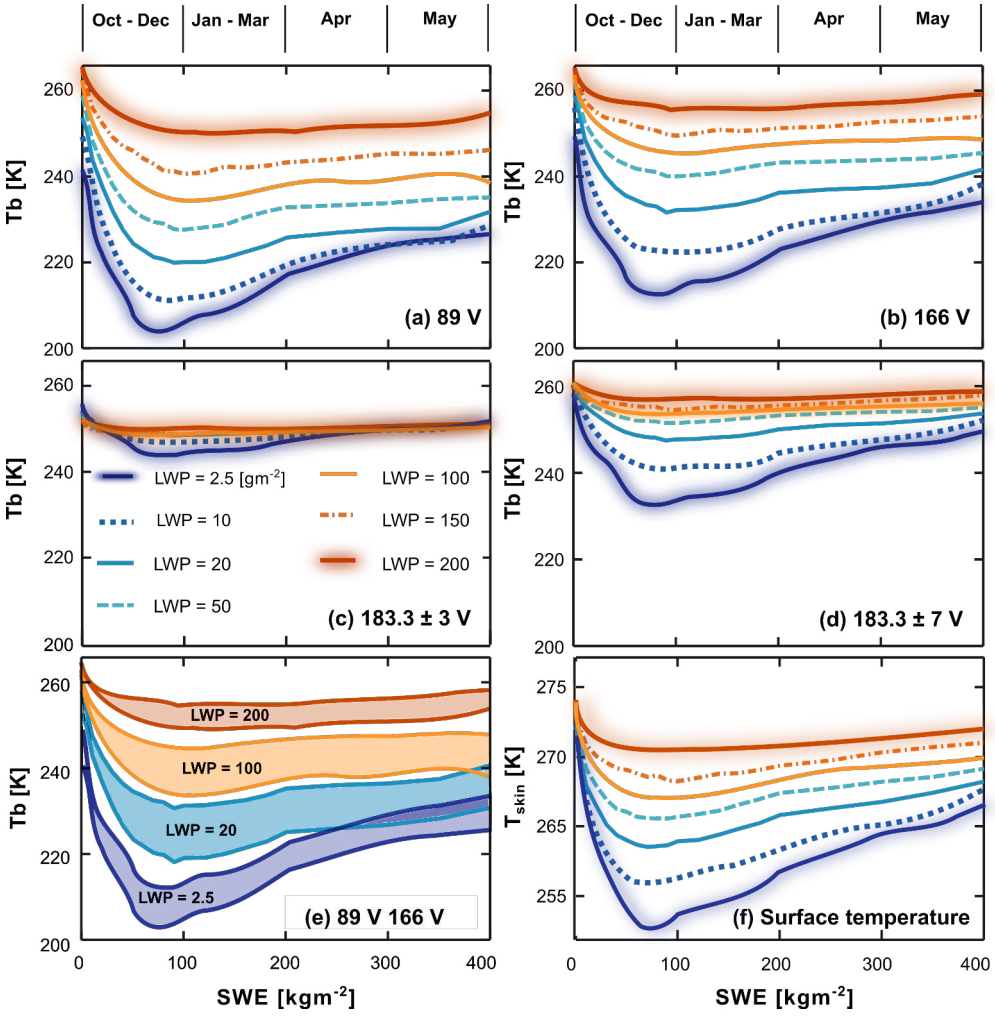

Figure 3. GMI high-frequency average Tb at channels 89V (a), 166V (b), 183±3 (c), and 183±7 GHz (d) as well as the comparison between the Tb values at 89 and 166 GHz (e) and average T_{skin} (f). All Tbs are for non-precipitating scenes. Also, the time at the top of the TB curves is the average time of the year corresponding to the average calculated SWE value.

4. The Snow Cover Emissivity Under Clear Sky

The microwave signal reaching the top of the atmosphere is the combination of the surface signal and the atmospheric contributions. If the atmospheric contribution becomes small enough to be ignored, we can easily calculate the surface emissivity (ε_s) as follows as also used by [63,64] and evaluated by [65]:

$$\varepsilon_s = \frac{\mathrm{Tb_s}}{\mathrm{T_{skin}}} \quad (1)$$

where $\mathrm{Tb_s}$ are the brightness temperature observed at top of the atmosphere in clear-sky conditions and thus it accounts only for snow-cover land. To minimize the atmospheric contribution, we only consider clear-sky observations with zero LWP, zero IWP, and zero precipitation. The atmospheric WVP is still present and thus might affect ε_s in the 183.3 ± 3 and 183.3 ± 7 GHz channels [41], but can be ignored for other frequencies. Fig. 4 shows the emissivity of snow-covered surfaces calculated for clear-sky as a function (Equation 1) of SWE for GMI high-frequency channels (89 V, H, 166 V, H, 183.3 ± 3, and 183.3 ± 7 GHz). Overall, the clear-sky surface emissivity of H-pol is about 0.01 less than the V-pol one. Also, the calculated clear-sky emissivity of the low-frequency channels (10.6, 18.7, 23.8 and 36.5 GHz, shown in Fig. A1 (Appendix A), are very similar to what previous emissivity studies

Preprints (www.preprints.org) | NOT PEER-REVIEWED | Posted: 22 June 2021 doi:10.20944/preprints202106.0544.v1

found [23,66].

Fig. 4a and b shows that for SWE values smaller than $\sim$ 100 kgm^{-2} the sensitivity of the surface emissivity to the SWE increase is larger at 89 GHz compared to 166 GHz. This trend is reversed for SWE $\geq$ 100 kgm^{-2} with the 89 GHz emissivity reaching a plateau at around 0.83 for H-Pol and 0.86 for V-Pol. This indicates that the emissivity at channel 166 GHz provides a better response to a full dynamic range of SWE with a consistent ε_s decrease, while at 89 GHz it saturates at SWE $\sim$ 100 kgm^{-2} thus almost getting blind to any further increase in SWE. We expect that this blindness of channel 89 GHz to SWE mostly occurs over Pacific Coast Ranges of northern British Columbia, North East Canada, Ural Mountains, Kjolen Mountains of Norway, and Verkhoyansk range in Russian Far East (Fig. 1e) during Jan-May (Fig. 3).

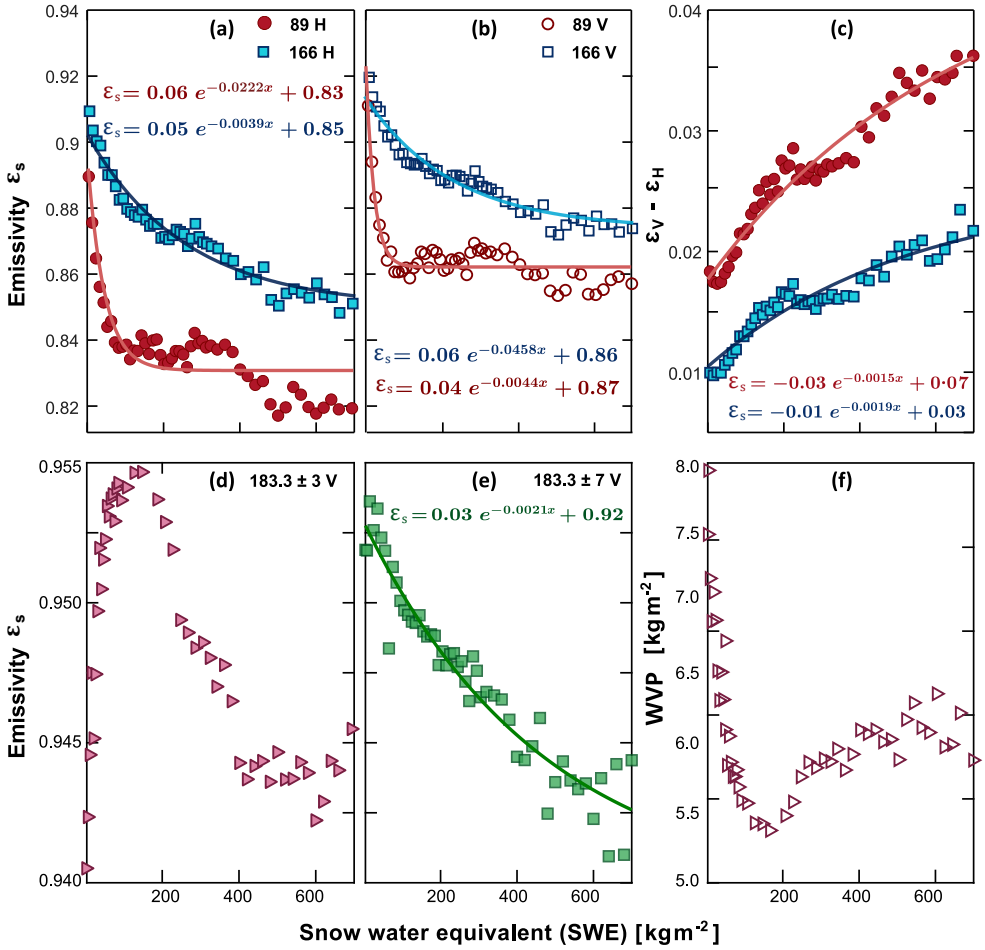

Figure 4. Clear-sky emissivity with snow water equivalent at GPM high-frequency channels (89 H & 166 H (a), 89 V & 166 V (b), 183$\pm$3 (d), and 183$\pm$7 (e)), the emissivity differences of V-pol and H-pol at 89 and 166 GHz frequencies (c), and the corresponding WVP (f). Note that the total cloud liquid water path, integrated total precipitable water, and ice water path in the column of atmosphere, and the near-surface precipitation are all zeros based on the data from both MERRA-2 model simulations and DPR ancillary database (2ADPR-ENV).

The variation of ε_s at water vapor channels (183.3 $\pm$ 3 and 183.3 $\pm$ 7 GHz) is very small ($\sim$ 0.015) and strongly anti-correlated with the variations of the atmospheric WVP (Fig. 4f). This is obviously due to the effects of the WVP in atmosphere masking the surface contribution. Therefore, hereafter in this paper, we only focus on the high-frequency window channels (89 V, H and 166 V, H GHz).

Our key observations on emissivity change rates in response to the increase in snow depth are summarized over the dry snow-covered surfaces after removing atmospheric contributions: (1) for SWE less than 10 kgm^{-2} the decreasing rate of emissivity at 89 GHz

Preprints (www.preprints.org) | NOT PEER-REVIEWED | Posted: 22 June 2021 doi:10.20944/preprints202106.0544.v1

exceeds that at 166 GHz and on the contrary, (2) for SWE greater than 100 kgm^{-2} the snow cover emissivity decays at a much higher rate at 166 GHz compared to 89 GHz. Although the 89 GHz emissivity of the surface covered with dry snowpack reaches a plateau for SWE$\geq$ 100 kgm^{-2} , it remains significantly lower than the non-plateaued emissivity at 166 GHz. This low emissivity can better capture the emission signal of snowfall which we analyze in the next two Sections.

5. Effects of Cloud Liquid Water Emission on Snow Cover Emissivity

Tb values at high-frequency channels may increase during snowfall events if clouds contain some liquid or supercooled water, which could completely mute the scattering contribution of snowfall [6,22,38,67,68]. Therefore, it is crucial to quantify the mixing effects of SWE scattering and thermal emission of LWP on the snowfall signal. We calculate the emissivity for different combinations of SWE and LWP in absence of precipitation. We compute the emissivity due to the LWP emission, assuming that the observed Tb (Tb_{obs}) is the sum of the clear-sky Tb ($Tb_s = \varepsilon_s \cdot T_{skin}$ from Equation 1) and the Tb due to the atmospheric LWP (Tb_{lwp}) as:

$$\begin{aligned} Tb_{obs} &= Tb_s + Tb_{lwp} \\ Tb_{obs} &= \varepsilon_s T_{skin} + \varepsilon_{lwp} T_{air} \end{aligned} \tag{2}$$

where ε_{lwp} is the emissivity due to the cloud liquid water, ε_s is the snow-cover emissivity under clear sky, and T_{air} is the air temperature. Therefore, the emissivity due to the LWP emission can be calculated as follow according to Equation 2:

$$\varepsilon_{lwp} = \frac{Tb_{obs} - \varepsilon_s T_{skin}}{T_{air}} \tag{3}$$

The calculated ε_{lwp} by Equation 3 are presented in Fig. 5. Here, ε_s is calculated for each SWE value using the regressed relationships shown in Fig. 4 computed from Equation 1.

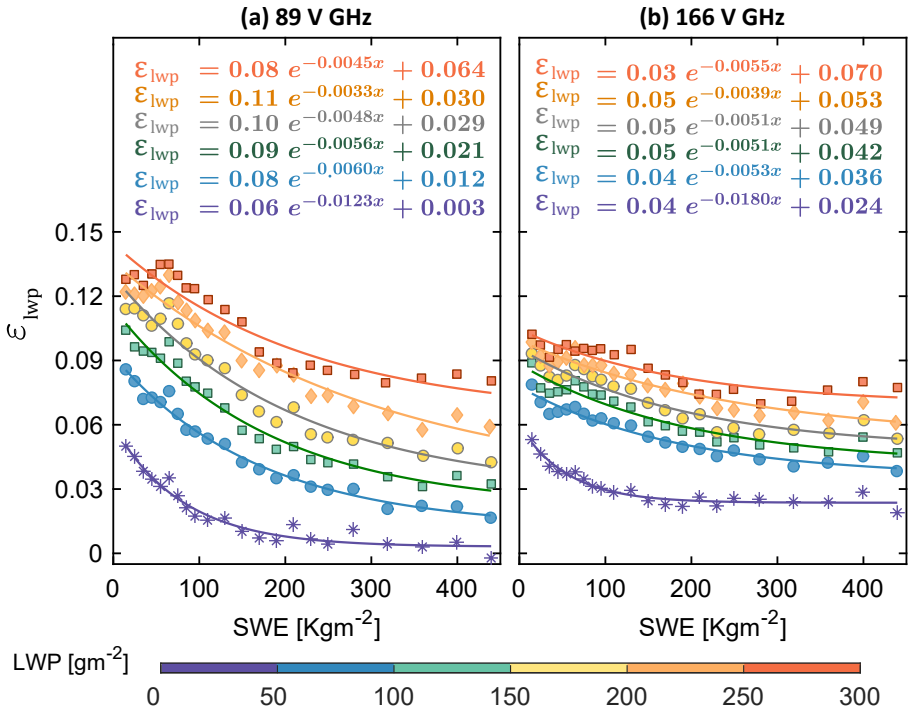

Figure 5. The atmosphere emissivity due to the cloud liquid water path (ε_{lwp}) against the snow cover water equivalent (SWE). The lines represent the best fit for each LWP interval shown in the colorbar.

Preprints (www.preprints.org) | NOT PEER-REVIEWED | Posted: 22 June 2021 doi:10.20944/preprints202106.0544.v1

The increase of LWP (from bottom to top curves) increases the atmospheric emissivity, and this variation can be significantly better captured at 89 GHz than 166 GHz (Fig. 5). This is because the 89 GHz clear sky emissivity (Fig. 4a,b) is lower than the 166 GHz one which allows the 89 GHz channel to have a more pronounced response when adding the emission contribution of LWP over SWE compared to channel 166 GHz. However, Fig. 5a shows that this contribution progressively decreases and becomes very small (~ 0.005) for LWP $\geq$ 200 gm^{-2}. These large values of LWP as observed in Fig. 2d occur mostly over Appalachian Mountains, the west coast of British Columbia, Alaska, and Northern Europe. On the contrary, at channel 166 GHz the LWP emissivity contribution shows a noticeable increase (~ 0.03) only for LWP values up to about 100 gm^{-2}, while for higher values LWP needs to increase significantly to show a similar emissivity response (Fig. 5b). This observation is very critical for snowfall detection since the LWP, as observed in Fig. 2c, largely increases during snowfall events. Moreover, larger emission contributions from clouds could mask the variations of surface emissivity caused by different snow cover scattering, particularly at 166 GHz channel. We see both channels respond better to the scattering of snow cover for SWE values less than 100 kgm^{-2}. This is obvious in Fig. 5 as lines are steeper for LWP when SWE is less than $\sim$ 100 kgm^{-2}. Similar findings for WVP were also revealed by [18] about the water vapor increase in the column of the atmosphere that could mask the variations of radiometric response to surface temperature at frequencies $\geq$ 89 GHz.

6. The Interactions of Snowfall Scattering with Snow Cover and Cloud Liquid Water

Now that the SWE and LWP emissivities are quantified, the snowfall scattering signal can be isolated as follow:

$$\begin{aligned} \mathrm{Tb_{obs}} &= \mathrm{Tb_s} + \mathrm{Tb_a} \\ \mathrm{Tb_{obs}} &= \varepsilon_s \mathrm{T_{skin}} + \varepsilon_a \mathrm{T_{air}} \\ \varepsilon_a &= \varepsilon_{sr} + \varepsilon_{lwp} \end{aligned} \tag{4}$$

where $\mathrm{Tb_a}$ and ε_a are the atmospheric brightness temperature and atmospheric emissivity, respectively. Also, recall that $\mathrm{Tb_s}$ from Equation 1 is the Tb at the top of the atmosphere at clear-sky, which only accounts for snow-cover emissivity.

The calculated ε_a from Equation 4 is shown in Fig. 6 illustrates. It is worth noting that when sr = 0, ε_a and ε_{lwp} are equal. The difference between emissivities in Fig. 6 for sr $= 0$ and sr > 0 shows the snowfall scattering contribution reducing the ε_a as all of the curves have almost equal amount of liquid water content ($150 - 200$ gm^{-2}). This LWP interval is selected based on its high probability of occurrence shown in Fig. 2 to ensure an adequate sample size in each SWE interval (20 kgm^{-2}) and snowfall rate interval of $0 <$ sr ≤ 0.5, $0.5 <$ sr ≤ 1, and $1 <$ sr ≤ 4 mmh^{-1}. The reason we did not go beyond sr $= 4$ mmh^{-1} is that the sample size significantly reduced due to the lack of enough heavy snowfall events in each LWP and SWE interval.

The results in Fig. 6 show that for SWE values close to zero and the same amount of LWP, the snowfall signal with intensity $0 - 0.5$ mmh^{-1} reduces the ε_a at 89 GHz by about 27% (from 0.11, grey line to 0.08, red line – Fig. 6a) and at 166 GHz by $\sim$ 38% (from 0.09, grey curve to 0.055, red curve – Fig. 6b). At 89 GHz, this decrease in emissivity due to snowfall scattering decreases with SWE, with a gap of about 0.015 ($\sim$ 18%) for SWE $\sim$ 200 kgm^{-2} and less than 0.005 ($\sim$ 3%) for SWE greater than 400 kgm^{-2} (Fig. 6a). As illustrated in Fig. 4, for the clear sky emissivity at 89 GHz channel when the snow depth increases on the ground, the land surface emissivity becomes relatively small (0.83) and reaches a plateau. Therefore, the small snowfall scattering cannot reduce the emissivity any further. However, the snowfall with sr $1 <$ sr ≤ 4 mmh^{-1} can further decrease the emissivity by about 0.018 from 0.078 to 0.06 for SWE values of $<$ 40 kgm^{-2} and from 0.03

Preprints (www.preprints.org) | NOT PEER-REVIEWED | Posted: 22 June 2021 doi:10.20944/preprints202106.0544.v1

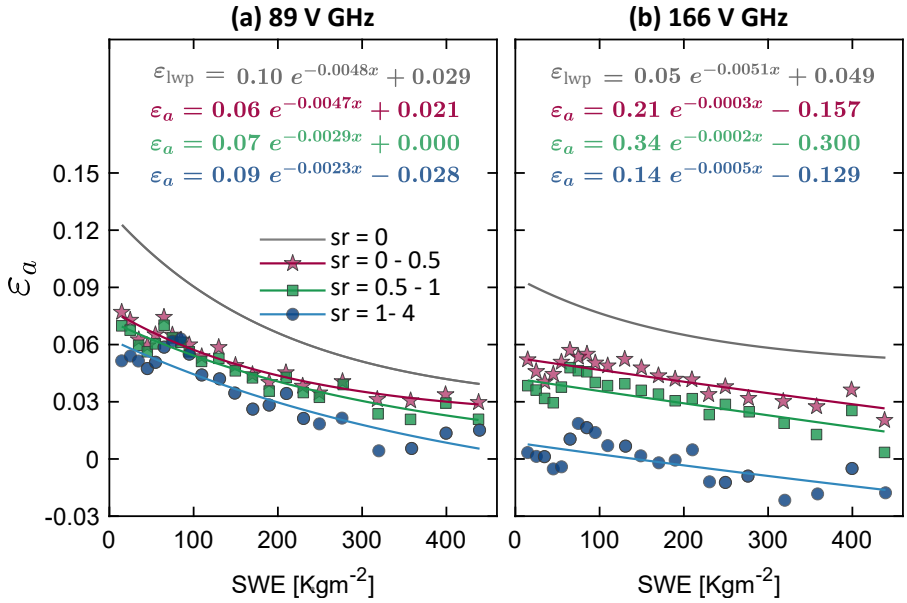

Figure 6. Atmospheric emissivity, (ε_a) for different snowfall rate intervals over dry snow cover for LWP $= 150 - 200$ gm^{-2} at 89 GHz (a) and 166 GHz (b). Note that the dark gray curve is associated with sr = 0 mmh^{-1}, which is the exact same curve (solid dark gray with yellow markers) in Fig. 5. It is shown here again for making comparisons of ε_a when sr > 0 and ε_{lwp} easier.

to about 0.01 at SWE values larger than 400 kgm^{-2} (the difference between red and blue curves, Fig. 6a).

For channel 166 GHz, Fig. 6b shows that the snowfall scattering contribution (refers to the emissivity decreases due to snowfall scattering) is almost the same as that of 89 GHz when the intensity is small (27% , sr ≤ 0.5 mmh^{-1}). However, channel 166 GHz responds more strongly to the increase in snowfall rate showing clearly separated curves for different sr intervals. The snowfall scattering contribution when $1 <$ sr ≤ 4 mmh^{-1} can further decrease the emissivity by about 0.06 (difference between the red and blue curves $\sim$ 96%) at channel 166 GHz compared with only 0.018 at channel 89 GHz ($\sim$ 23%).

7. Discussion

By integrating the findings from Fig. 5 and Fig. 6, we conclude that for small snowfall intensities ($\leq$ 0.5 mmh^{-1}) over shallow snow cover (SWE $<$ 100 kgm^{-2}), LWP values even as small as 0–50 gm^{-2} could increase the emissivity by 0.02–0.05 and thus, could completely mask the scattering contribution of snowfall ($\sim$0.05 as a difference between ε_{lwp} and ε_a) at channel 89 GHz. Larger snowfall rates might be only captured at small LWP values. The 166 GHz channel could still capture some snowfall scattering at SWE values less than 100 kgm^{-2}, defeating the emissivity increase of small liquid water content. However, the snowfall scattering contribution is masked also at this channel when the LWP becomes larger than 100–150 gm^{-2}, which increases the emissivity by almost more than about 0.07.

Over deeper snow cover with SWE larger than 100 kgm^{-2}, the snow cover scattering contribution becomes very significant and thus, alleviates the contribution from the small intensities of snowfall scattering, making them no longer distinguishable from the background emissivity at both 89 GHz and 166 GHz channels. Larger snowfall intensities (1–4 mmh^{-1}) still decrease the background surface emissivity even over deep snow cover with SWE $\geq$ 100 kgm^{-2} at 89 GHz channel for LWP values up to 50-100 gm^{-2}, but are masked for larger LWP values. This is because the decrease in emissivity due to the increased snowfall rate (Fig. 6a) is lower than the increase in emissivity because of the increased emission of LWP (Fig. 5a). At 166 GHz, both SWE scattering and LWP emission

Preprints (www.preprints.org) | NOT PEER-REVIEWED | Posted: 22 June 2021 doi:10.20944/preprints202106.0544.v1

over deep snow-covered surfaces are relatively smaller than those at 89 GHz. Therefore, the 166 GHz channel is more capable of capturing the snowfall scattering signal with large intensities (sr>1 mmh^{-1}) for LWP values up to 100–150 gm^{-2}.

For larger LWP values ($\sim > 150$ gm^{-2}) over regions with SWE ≥ 100 kgm^{-2}, it is revealed that the snowfall signal could be captured by its emission signature — LWP increase during snowfall events — instead of its scattering signature at channel 89 GHz. This is because the surface emissivity at channel 89 GHz reaches a plateau value and remains unchanged to further increase in SWE. Therefore, over regions with deep snow cover, the 89 GHz channel could capture this emission signal of the snowy clouds for snowfall detection. The challenging land-atmospheric situations for snowfall retrieval particularly occur if there is not any scattering nor emission signal which is when LWP $> 100 - 150$ gm^{-2} and SWE < 100 kgm^{-2}.

In the present article, the relations between Tbs, snowfall, cloud liquid water with emphasis on snow-covered regions were established as multi-year averages from four years of colocated GPM and MERRA-2 reanalysis data. The immediate goal here was to investigate the challenging zones of snowfall retrieval over the snow cover at high-frequency GPM channels regarding the confounding effects of these atmospheric constituents over the snow-covered regions. However, at the daily or sub-daily time scales, large variability around these multi-year averages is expected. When seeking to establish relationships at these finer time scales, the temporal variability needs to be either handled as a stochastic process or analysed in relation to additional physical parameters which have not been taken into account in the present study (e.g. snow density and wetness, particles shape and size distribution, etc). Additionally, at fine time scales, significant variability is expected to be related to errors and inaccuracies in the measured/estimated variables in both satellite observations and reanalysis products.

For instantaneous precipitation retrievals, one should consider the use of the dynamic surface emissivity database developed by [69] and evaluated in GPM retrieval by [70], which implements the optimal estimation method with a forward model error covariance matrix. Future research would benefit from using this dynamic land surface emissivity database for further investigation of the findings of the present paper and for establishing relationships between LWP, SWE, and snowfall at finer temporal scales.

The fact that GMI and the DPR are flying onboard the same platform allows for a high number of colocated observations at all latitudes; however, we acknowledge potential errors and inaccuracies in DPR measurements regarding light precipitation intensities. An additional investigation, if it does not require high space-time coverage, should consider measurements from CloudSat Cloud Profiling Radar (CPR), which is known to more accurately capture low-intensity snowfall [71,72].

In this study we only used total precipitable water to screen the clear-sky Tbs. This can add some uncertainties regarding the calculated emissivities of LWP and snowfall. Future research needs to investigate the effects of total precipitable water on the radiometric signal during the snowfall events [73].

8. Conclusions

We analyzed snow cover effects on the snowfall radiometric signal under different snow water equivalent and liquid water content of clouds, by considering the effect of surface temperature variations, as well. To isolate the surface temperature thermal emissivity, we first calculated the clear-sky emissivity. Then, we computed the contribution of scattering and emission from the other mentioned land-atmospheric constituents directly by comparing their emissivity with clear-sky snow cover emissivity. We found that the channel 166 GHz could better capture the scattering signature of light snowfall events because it responds less strongly to the increase of the cloud liquid water than the 89 GHz channel. Larger snowfall events could be captured better at 89 GHz when both LWP and SWE are small, while 166 GHz becomes more advantageous at capturing this scattering when LWP increases up to about 100–150 gm^{-2}. Over deeper snow-cover regions,

Preprints (www.preprints.org) | NOT PEER-REVIEWED | Posted: 22 June 2021 doi:10.20944/preprints202106.0544.v1

and particularly larger LWP values ($\geq 100 - 150$ gm^{-2}), the scattering of snowfall, even with large intensity, is masked by the comparable scattering contribution from the large accumulation of snow cover and the emission from liquid water at both 89 and 166 GHz channels. At this land-atmospheric condition, the snowfall dominant signature becomes its emission that can be distinguished from the very low plateaued emissivity of the surface at channel 89 GHz. We believe that a quantitative climatological assessment such as this presented herein can provide useful information for improving passive microwave retrieval of snowfall and also serve as diagnostics for interpreting the bias and uncertainty of current products.

Author Contributions: Methodology, formal analysis, investigation, data curation, visualization, and writing of the original draft: Z. Takbiri. Extensive editing: L. Milani. Conceptualization, reviewing and editing: Z. Takbiri, L. Milani, C. Guilloteau and E. Foufoula-Georgiou. Funding acquisition: E. Foufoula-Georgiou. All authors have read and agreed to the published version of the manuscript.

Funding: Authors acknowledge the support from the National Aeronautics and Space Administration (NASA) Precipitation Measurement Mission (PMM) GPM program (grant 80NSSC19K0684). Dr. Lisa Milani has been funded by the NASA GPM Mission.

Data Availability Statement: The GPM data are provided courtesy of the NASA Precipitation Processing System at the Goddard Space Flight Center (https://pmm.nasa.gov/data-access/). The MERRA-2 data are from the Goddard Earth Sciences and Information Service Center (https://disc.sci.gsfc.nasa.gov/mdisc/). The IMS snow cover product is available at United States National Ice Center (ftp://sidads.colorado.edu/pub/DATASETS/NOAA/G02156/). All colocated GMI, SWE, LWP, WVP, TPW, *sr* from DPR, T_{skin}, T_{air}, and T_{2m} at DPR resolution and calculated emissivity data ε_s, ε_{LWT}, and ε_a are available upon request.

Acknowledgments: The authors would like to thank Dr. F. Joseph Turk from the Jet Propulsion Laboratory, Dr. Gail Skofronick-Jackson from NASA HQ and Dr. Ardeshir Ebtehaj from St. Anthony Falls laboratory at University of Minnesota for their valuable discussion and feedback at the early stage of this research.

Conflicts of Interest: The authors declare no conflict of interest.

Appendix A

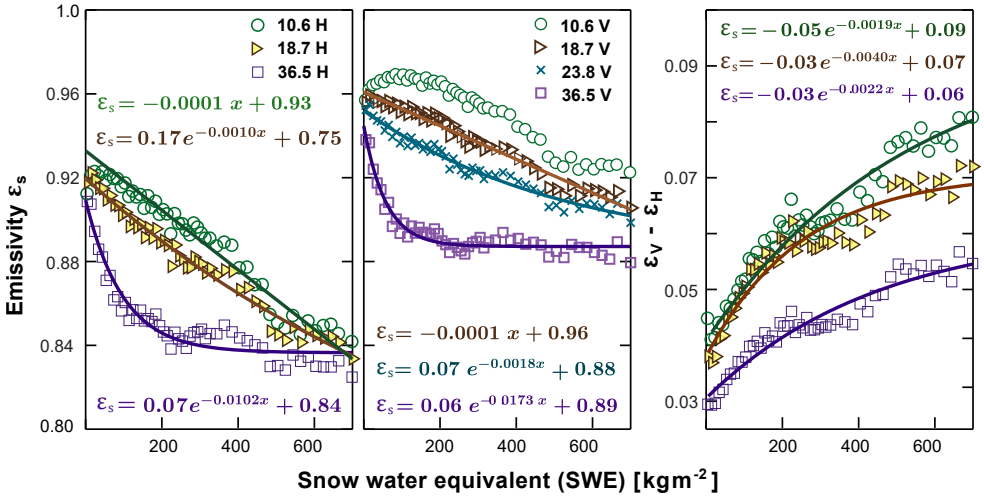

Figure A1. Clear-sky emissivity with snow water equivalent at GPM low-frequency channels (10.6, 18.7, and 36.5 GHz V, H) and the emissivity differences of V-pol and H-pol. Note that the total cloud liquid water path, integrated total precipitable water, and ice water path in the column of atmosphere, and the near-surface precipitation are all zeros based on the data from both MERRA-2 model simulations and DPR ancillary database (2ADPR-ENV).

References

1. Skofronick-Jackson, G.; Kim, M.J.; Weinman, J.; Chang, D.E. A physical model to determine snowfall over land by microwave radiometry. *IEEE Transactions on Geoscience and Remote Sensing* **2004**, *42*, 1047–1058. doi:10.1109/TGRS.2004.825585.
2. Noh, Y.J.J.; Liu, G.; Jones, A.S.; Haar, T.H.V.; Vonder Haar, T.H. Toward snowfall retrieval over land by combining satellite and in situ measurements. *Journal of Geophysical Research Atmospheres* **2009**, *114*, 1–15. doi:10.1029/2009JD012307.
3. Kidd, C.; Shige, S.; Vila, D.; Tarnavsky, E.; Yamamoto, M.K.; Maggioni, V.; Maseko, B. The IPWG Satellite Precipitation Validation Effort. In *Satellite Precipitation Measurement*; Springer, 2020; pp. 453–470.
4. Massari, C.; Maggioni, V. Error and Uncertainty Characterization. In *Satellite Precipitation Measurement*; Springer, 2020; pp. 515–532.
5. Tang, G.; Clark, M.P.; Papalexiou, S.M.; Ma, Z.; Hong, Y. Have satellite precipitation products improved over last two decades? A comprehensive comparison of GPM IMERG with nine satellite and reanalysis datasets. *Remote Sensing of Environment* **2020**, *240*, 111697.
6. Mroz, K.; Montopoli, M.; Battaglia, A.; Panegrossi, G.; Kirstetter, P.; Baldini, L. Cross-validation of active and passive microwave snowfall products over the continental United States. *Journal of Hydrometeorology* **2021**.
7. Kummerow, C.D.; Randel, D.L.; Kulie, M.; Wang, N.Y.; Ferraro, R.; Joseph Munchak, S.; Petkovic, V. The evolution of the goddard profiling algorithm to a fully parametric scheme. *Journal of Atmospheric and Oceanic Technology* **2015**, *32*, 2265–2280. doi:10.1175/JTECH-D-15-0039.1.
8. Petty, G.W.; Huang, W.; Petty, G.W.; Huang, W. Microwave Backscatter and Extinction by Soft Ice Spheres and Complex Snow Aggregates. *Journal of the Atmospheric Sciences* **2010**, *67*, 769–787. doi:10.1175/2009JAS3146.1.
9. Skofronick-Jackson, G.; Johnson, B.T. Surface and atmospheric contributions to passive microwave brightness temperatures for falling snow events. *Journal of Geophysical Research* **2011**, *116*, D02213. doi:10.1029/2010JD014438.
10. Munchak, S.J.; Skofronick-Jackson, G. Evaluation of precipitation detection over various surfaces from passive microwave imagers and sounders. *Atmospheric Research* **2013**, *131*, 81 – 94. Perspectives of Precipitation Science - Part I, doi:https://doi.org/10.1016/j.atmosres.2012.10.011.
11. Libbrecht, K.G. Morphogenesis on ice: The physics of snow crystals. *Engineering and Science* **2001**, *64*, 10–19.
12. Gravner, J.; Griffeath, D. Modeling snow-crystal growth: A three-dimensional mesoscopic approach. *Phys. Rev. E* **2009**, *79*, 011601. doi:10.1103/PhysRevE.79.011601.
13. Pruppacher, H.R.; Klett, J.D. *Microphysics of Clouds and Precipitation: Reprinted 1980*; Springer Science & Business Media, 2012.
14. Libbrecht, K.G. Physical Dynamics of Ice Crystal Growth. *Annual Review of Materials Research* **2017**, *47*, 271–295. doi:10.1146/annurev-matsci-070616-124135.
15. Meng, H.; Dong, J.; Ferraro, R.; Yan, B.; Zhao, L.; Kongoli, C.; Wang, N.Y.; Zavodsky, B. A 1DVAR-based snowfall rate retrieval algorithm for passive microwave radiometers. *Journal of Geophysical Research: Atmospheres* **2017**, *122*, 6520–6540.
16. Liu, G. A Database of Microwave Single-Scattering Properties for Nonspherical Ice Particles. *Bulletin of the American Meteorological Society* **2008**, *89*, 1563–1570. doi:10.1175/2008BAMS2486.1.
17. Bennartz, R.; Bauer, P. Sensitivity of microwave radiances at 85-183 GHz to precipitating ice particles. *Radio Science* **2003**, *38*, –. doi:10.1029/2002RS002626.
18. You, Y.; Wang, N.Y.; Ferraro, R.; Rudlosky, S. Quantifying the Snowfall Detection Performance of the GPM Microwave Imager Channels over Land. *Journal of Hydrometeorology* **2017**, *18*, 729–751. doi:10.1175/JHM-D-16-0190.1.
19. Liu, G.; Curry, J.A. Observation and interpretation of microwave cloud signatures over the Arctic Ocean during winter. *Journal of Applied Meteorology* **2003**, *42*, 51–64.
20. Wang, Y.; Liu, G.; Seo, E.K.; Fu, Y. Liquid water in snowing clouds: Implications for satellite remote sensing of snowfall. *Atmospheric Research* **2013**, *131*, 60–72. doi:10.1016/j.atmosres.2012.06.008.
21. Kulie, M.S.; Bennartz, R.; Greenwald, T.J.; Chen, Y.; Weng, F. Uncertainties in Microwave Properties of Frozen Precipitation: Implications for Remote Sensing and Data Assimilation. *Journal of the Atmospheric Sciences* **2010**, *67*, 3471–3487. doi:10.1175/2010JAS3520.1.

22. Liu, G.; Seo, E.K. Detecting snowfall over land by satellite high-frequency microwave observations: The lack of scattering signature and a statistical approach. *Journal of geophysical research: atmospheres* **2013**, *118*, 1376–1387.
23. Ulaby, F.T.; Stiles, W.H. The active and passive microwave response to snow parameters: 2. Water equivalent of dry snow. *Journal of Geophysical Research: Oceans* **1980**, *85*, 1045–1049. doi: 10.1029/JC085iC02p01045.
24. Mätzler, C. Passive microwave signatures of landscapes in winter. *Meteorology and Atmospheric Physics* **1994**, *54*, 241–260. doi:10.1007/BF01030063.
25. Hallikainen, M.T. Microwave radiometry of snow. *Advances in Space Research* **1989**, *9*, 267–275. doi:10.1016/0273-1177(89)90494-8.
26. Foster, J.L.; Hall, D.K.; Chang, A.T.C.; Rango, A. An overview of passive microwave snow research and results. *Reviews of Geophysics* **1984**, *22*, 195–208. doi:10.1029/RG022i002p00195.
27. Grody, N.C. Relationship between snow parameters and microwave satellite measurements: Theory compared with Advanced Microwave Sounding Unit observations from 23 to 150 GHz. *Journal of Geophysical Research: Atmospheres* **2008**, *113*, –. doi:10.1029/2007JD009685.
28. Colbeck, S.C. An overview of seasonal snow metamorphism. *Reviews of Geophysics* **1982**, *20*, 45–61. doi:10.1029/RG020i001p00045.
29. E. Schanda, C.M.; Kunzi, K. Microwave remote sensing of snow cover. *International Journal of Remote Sensing* **1983**, *4*, 149–158. doi:10.1080/01431168308948536.
30. Rosenfeld, S.; Grody, N. Anomalous microwave spectra of snow cover observed from Special Sensor Microwave/Imager measurements. *Journal of Geophysical Research: Atmospheres* **2000**, *105*, 14913–14925. doi:10.1029/1999JD900486.
31. Foster, J.L.; Skofronick-Jackson, G.; Meng, H.; Wang, J.R.; Riggs, G.; Kocin, P.J.; Johnson, B.T.; Cohen, J.; Hall, D.K.; Nghiem, S.V. Passive microwave remote sensing of the historic February 2010 snowstorms in the Middle Atlantic region of the USA. *Hydrological Processes* **2012**, *26*, 3459–3471. doi:10.1002/hyp.8418.
32. Chang, A.T.C.; Gloersen, P.; Schmugge, T.; Wilheit, T.T.; Zwally, H.J. Microwave emission from snow and glacier ice. *Journal of Glaciology* **1976**, *16*, 23 –39. doi:10.1017/S0022143000031415.
33. Pulliainen, J.; Hallikainen, M. Retrieval of regional snow water equivalent from space-borne passive microwave observations. *Remote Sensing of Environment* **2001**, *75*, 76–85. doi:10.1016/S0034-4257(00)00157-7.
34. Stiles, W.H.; Ulaby, F.T. The active and passive microwave response to snow parameters: 1. Wetness. *Journal of Geophysical Research* **1980**, *85*, 1037. doi:10.1029/JC085iC02p01037.
35. Grody, N.C. Classification of snow cover and precipitation using the special sensor microwave imager. *Journal of Geophysical Research* **1991**, *96*, 7423. doi:10.1029/91JD00045.
36. Stephens, G.L.; Kummerow, C.D. The Remote Sensing of Clouds and Precipitation from Space: A Review. *Journal of the Atmospheric Sciences* **2007**, *64*, 3742–3765. doi:10.1175/2006JAS2375.1.
37. Ebtehaj, A.M.; Kummerow, C.D. Microwave retrievals of terrestrial precipitation over snow-covered surfaces: A lesson from the GPM satellite. *Geophysical Research Letters* **2017**, *44*, 6154–6162. doi:10.1002/2017GL073451.
38. Panegrossi, G.; Rysman, J.F.; Casella, D.; Marra, A.C.; Sanò, P.; Kulie, M.S. CloudSat-based assessment of GPM Microwave Imager snowfall observation capabilities. *Remote Sensing* **2017**, *9*, 1263.
39. Takbiri, Z.; Ebtehaj, A.; Foufoula-Georgiou, E.; Kirstetter, P.E.; Turk, F.J. A Prognostic Nested k-Nearest Approach for Microwave Precipitation Phase Detection over Snow Cover. *Journal of Hydrometeorology* **2019**, *20*, 251–274. doi:10.1175/JHM-D-18-0021.1.
40. Burgard, C.; Notz, D.; Pedersen, L.T.; Tonboe, R.T. The Arctic Ocean Observation Operator for 6.9 GHz (ARC3O)–Part 1: How to obtain sea ice brightness temperatures at 6.9 GHz from climate model output. *The Cryosphere* **2020**, *14*, 2369–2386.
41. Kim, M.J.; Weinman, J.A.; Olson, W.S.; Chang, D.E.; Skofronick-Jackson, G.; Wang, J.R. A physical model to estimate snowfall over land using AMSU-B observations. *Journal of Geophysical Research* **2008**, *113*, D09201. doi:10.1029/2007JD008589.
42. Liu, G. Deriving snow cloud characteristics from CloudSat observations. *Journal of Geophysical Research Atmospheres* **2008**, *114*, 1–13. doi:10.1029/2007JD009766.
43. You, Y.; Wang, N.Y.; Ferraro, R. A prototype precipitation retrieval algorithm over land using passive microwave observations stratified by surface condition and precipitation vertical structure. *Journal of Geophysical Research: Atmospheres* **2015**, *120*, 5295–5315. 2014JD022534, doi: 10.1002/2014JD022534.

44. Skofronick-Jackson, G.M.; Gasiewski, A.J.; Wang, J.R. Influence of microphysical cloud parameterizations on microwave brightness temperatures. *IEEE Transactions on Geoscience and Remote Sensing* **2002**, *40*, 187–196. doi:10.1109/36.981360.
45. Levizzani, V.; Kidd, C.; Aonashi, K.; Bennartz, R.; Ferraro, R.; Huffman, G.R.; Roca, R.; Turk, F.; Wang, N.Y. The activities of the International Precipitation Working Group. *Quarterly Journal of the Royal Meteorological Society* **2018**, *0*. doi:10.1002/qj.3214.
46. Levizzani, V.; Laviola, S.; Cattani, E. Detection and measurement of snowfall from space. *Remote Sensing* **2011**, *3*, 145–166. doi:10.3390/rs3010145.
47. Mätzler, C.; Rosenkranz, P.W.; Cermak, J. Microwave absorption of supercooled clouds and implications for the dielectric properties of water. *Journal of Geophysical Research: Atmospheres* **2010**, *115*. doi:10.1029/2010JD014283.
48. Mätzler, C. Improved Born approximation for scattering of radiation in a granular medium. *J. Appl. Phys.* **1998**, *83*, 6111. doi:10.1063/1.367496.
49. Polder, D.; van Santen, J. The effective permeability of mixtures of solids. *Physica* **1946**, *12*, 257–271. doi:10.1016/S0031-8914(46)80066-1.
50. Iguchi, T.; Seto, S.; Meneghini, R.; Yoshida, N.; Awaka, J.; Kubota, T. GPM/DPR Level-2 Algorithm Theoretical Basis Document Authors. Technical report, NASA Goddard Space Flight Center, Greenbelt, MD, USA, 2010. Available online at https://pmm.nasa.gov/sites/default/files/document_files/ATBD_GPM_DPR_n3_dec15.pdf.
51. Hou, A.Y.; Kakar, R.K.; Neeck, S.; Azarbarzin, A.A.; Kummerow, C.D.; Kojima, M.; Oki, R.; Nakamura, K.; Iguchi, T. The global precipitation measurement mission. *Bulletin of the American Meteorological Society* **2014**, *95*, 701–722. doi:10.1175/BAMS-D-13-00164.1.
52. Skofronick-Jackson, G.; Petersen, W.A.; Berg, W.; Kidd, C.; Stocker, E.F.; Kirschbaum, D.B.; Kakar, R.; Braun, S.A.; Huffman, G.J.; Iguchi, T.; Kirstetter, P.E.; Kummerow, C.; Meneghini, R.; Oki, R.; Olson, W.S.; Takayabu, Y.N.; Furukawa, K.; Wilheit, T. The global precipitation measurement (GPM) mission for science and Society. *Bull. Am. Meteorol. Soc.* **2017**. doi:10.1175/BAMS-D-15-00306.1.
53. Hamada, A.; Takayabu, Y.N. Improvements in Detection of Light Precipitation with the Global Precipitation Measurement Dual-Frequency Precipitation Radar (GPM DPR). *Journal of Atmospheric and Oceanic Technology* **2016**, *33*, 653–667. doi:10.1175/JTECH-D-15-0097.1.
54. Kidd, C.; Huffman, G. Global precipitation measurement. *Meteorological Applications* **2011**, *18*, 334–353. doi:10.1002/met.284.
55. Gelaro, R.; McCarty, W.; Suárez, M.J.; Todling, R.; Molod, A.; Takacs, L.; Randles, C.A.; Darmenov, A.; Bosilovich, M.G.; Reichle, R.; Wargan, K.; Coy, L.; Cullather, R.; Draper, C.; Akella, S.; Buchard, V.; Conaty, A.; da Silva, A.M.; Gu, W.; Kim, G.K.; Koster, R.; Lucchesi, R.; Merkova, D.; Nielsen, J.E.; Partyka, G.; Pawson, S.; Putman, W.; Rienecker, M.; Schubert, S.D.; Sienkiewicz, M.; Zhao, B.; Gelaro, R.; McCarty, W.; Suá rez, M.J.; Todling, R.; Molod, A.; Takacs, L.; Randles, C.A.; Darmenov, A.; Bosilovich, M.G.; Reichle, R.; Wargan, K.; Coy, L.; Cullather, R.; Draper, C.; Akella, S.; Buchard, V.; Conaty, A.; da Silva, A.M.; Gu, W.; Kim, G.K.; Koster, R.; Lucchesi, R.; Merkova, D.; Nielsen, J.E.; Partyka, G.; Pawson, S.; Putman, W.; Rienecker, M.; Schubert, S.D.; Sienkiewicz, M.; Zhao, B. The Modern-Era Retrospective Analysis for Research and Applications, Version 2 (MERRA-2). *Journal of Climate* **2017**, *30*, 5419–5454. doi:10.1175/JCLI-D-16-0758.1.
56. U.S. National Ice Center. 2008, updated daily. IMS Daily Northern Hemisphere Snow and Ice Analysis at 1 km, 4 km, and 24 km Resolutions, Version 1. Jan 2015-Dec2021. *Boulder, Colorado USA. NSIDC: National Snow and Ice Data Center.* doi:https://doi.org/10.7265/N52R3PMC.
57. Suarez, M.J.; daSilva, A.; Dee, D.; Bloom, S.; Bosilovich, M.; Pawson, S.; Schubert, S.; Wu, M.L.; Sienkiewicz, M.; Stajner, I. Documentation and validation of the Goddard Earth Observing System (GEOS) data assimilation system, version 4. GLIMS Technical Report 9788578110796,1098-6596, Global Land Ice Measurements from Space, oulder Colorado, USA, 2005.
58. Gultepe, I.; Isaac, G. Liquid water content and temperature relationship from aircraft observations and its applicability to GCMs. Technical Report 3, 1997. doi:https://doi.org/10.1175/1520-0442(1997)010<0446:LWCATR>2.0.CO;2.
59. Kubota, T.; Satoh, M.; Nasuno, T.; Seto, S.; Iguchi, T.; Oki, R. Development of cloud liquid water database using global cloud-system resolving model for GPM/DPR algorithm. 2012 IEEE International Geoscience and Remote Sensing Symposium, 2012, pp. 350–353. doi:10.1109/IGARSS.2012.6351566.
60. Davis, R.E.; Lowit, M.B.; Knappenberger, P.C.; Legates, D.R. A climatology of snowfall-temperature relationships in Canada. *Journal of Geophysical Research: Atmospheres* **1999**, *104*, 11985–11994. doi:10.1029/1999JD900104.

61. Hewison, T.J.; English, S.J. Airborne retrievals of snow and ice surface emissivity at millimeter wavelengths. *IEEE Transactions on Geoscience and Remote Sensing* **1999**, *37*, 1871–1879. doi: 10.1109/36.774700.
62. Hu, Y.; Rodier, S.; Xu, K.m.; Sun, W.; Huang, J.; Lin, B.; Zhai, P.; Josset, D. Occurrence, liquid water content, and fraction of supercooled water clouds from combined CALIOP/IIR/MODIS measurements. *Journal of Geophysical Research: Atmospheres* **2010**, *115*, n/a–n/a. D00H34, doi: 10.1029/2009JD012384.
63. Prigent, C.; Aires, F.; Rossow, W.B. Land Surface Microwave Emissivities over the Globe for a Decade. *Bulletin of the American Meteorological Society* **2006**, *87*, 1573 – 1584. doi:10.1175/BAMS-87-11-1573.
64. Prigent, C.; Rossow, W.B.; Matthews, E. Microwave land surface emissivities estimated from SSM/I observations. *Journal of Geophysical Research* **1997**, *102*, 21867–21890. doi:10.1002/1099-0690(200204)2002:7<1143::AID-EJOC1143>3.0.CO;2-G.
65. Ferraro, R.R.; Peters-Lidard, C.D.; Hernandez, C.; Turk, F.J.; Aires, F.; Prigent, C.; Lin, X.; Boukabara, S.A.; Furuzawa, F.A.; Gopalan, K.; Harrison, K.W.; Karbou, F.; Li, L.; Liu, C.; Masunaga, H.; Moy, L.; Ringerud, S.; Skofronick-Jackson, G.M.; Tian, Y.; Wang, N.Y. An Evaluation of Microwave Land Surface Emissivities Over the Continental United States to Benefit GPM-Era Precipitation Algorithms. *IEEE Transactions on Geoscience and Remote Sensing* **2013**, *51*, 378–398. doi:10.1109/TGRS.2012.2199121.
66. Chang, A.; Foster, J.; Hall, D. Nimbus-7 SMMR Derived Global Snow Cover Parameters. *Annals of Glaciology* **1987**, *9*, 39–44. doi:10.3189/S0260305500200736.
67. Kneifel, S.; Löhnert, U.; Battaglia, A.; Crewell, S.; Siebler, D. Snow scattering signals in ground-based passive microwave radiometer measurements. *Journal of Geophysical Research: Atmospheres* **2010**, *115*, n/a–n/a. D16214, doi:10.1029/2010JD013856.
68. Rysman, J.F.; Panegrossi, G.; Sanò, P.; Marra, A.C.; Dietrich, S.; Milani, L.; Kulie, M.S. SLALOM: An all-surface snow water path retrieval algorithm for the GPM Microwave Imager. *Remote Sensing* **2018**, *10*, 1278.
69. Munchak, S.J.; Ringerud, S.; Brucker, L.; You, Y.; de Gelis, I.; Prigent, C. An Active–Passive Microwave Land Surface Database From GPM. *IEEE Transactions on Geoscience and Remote Sensing* **2020**, *58*, 6224–6242. doi:10.1109/TGRS.2020.2975477.
70. Ringerud, S.; Peters-Lidard, C.; Munchak, J.; You, Y. Applications of Dynamic Land Surface Information for Passive Microwave Precipitation Retrieval. *Journal of Atmospheric and Oceanic Technology* **2021**, *38*, 167 – 180. doi:10.1175/JTECH-D-20-0048.1.
71. Casella, D.; Panegrossi, G.; Sanò, P.; Marra, A.C.; Dietrich, S.; Johnson, B.T.; Kulie, M.S. Evaluation of the GPM-DPR snowfall detection capability: Comparison with CloudSat-CPR. *Atmospheric Research* **2017**, *197*, 64–75. doi:https://doi.org/10.1016/j.atmosres.2017.06.018.
72. Turk, F.J.; Ringerud, S.E.; Camplani, A.; Casella, D.; Chase, R.J.; Ebtehaj, A.; Gong, J.; Kulie, M.; Liu, G.; Milani, L.; Panegrossi, G.; Padullés, R.; Rysman, J.F.; Sanò, P.; Vahedizade, S.; Wood, N.B. Applications of a CloudSat-TRMM and CloudSat-GPM Satellite Coincidence Dataset. *Remote Sensing* **2021**, *13*. doi:10.3390/rs13122264.
73. Milani, L.; Kulie, M.S.; Casella, D.; Kirstetter, P.E.; Panegrossi, G.; Petkovic, V.; Ringerud, S.E.; Rysman, J.F.; Sanò, P.; Wang, N.Y.; others. Extreme Lake-Effect Snow from a GPM Microwave Imager Perspective: Observational Analysis and Precipitation Retrieval Evaluation. *Journal of Atmospheric and Oceanic Technology* **2021**, *38*, 293–311.